JOURNAL OF GUIDANCE, CONTROL, AND DYNAMICS
Vol. 30, No. 1, January–February 2007

Innovative Navigation Schemes for State and Parameter Estimation During Mars Entry

Jean François Lévesque*
Universite de Sherbrooke, Sherbrooke, Quebec J1K 2R1, Canada
and
Jean de Lafontaine†
NGC Aerospace Ltd., Sherbrooke, Quebec J1J 2C3, Canada and Université de Sherbrooke, Sherbrooke, Quebec J1K 2R1, Canada

DOI: 10.2514/1.25107

Accurate navigation systems are required in the scope of Mars precision landing missions. This paper reviews some assumptions of the literature concerning the availability of the vehicle states for guidance during its atmospheric entry on Mars. It is demonstrated that currently used measurements are not sufficient to get complete observability of the entry dynamics. Therefore, four innovative measurement scenarios based on radio ranging are proposed to resolve the observability issue. The analyses and simulations show that the addition of the range measurements from known references helps to estimate accurately the position states along with some critical model parameters, contrary to inertial measurement unit navigation alone. Finally, the addition of the range measurement from a secondary free-falling dummy vehicle with known aerodynamics also ensures the observability of aerodynamic parameters of the lander vehicle.

Nomenclature

A, B, C, D	=	state-space matrices
$\mathbf{a}^B$	=	acceleration components in the body frame, m/s^2
B	=	ballistic parameter, m^2/kg
C_D	=	aerodynamic drag coefficient
C_L	=	aerodynamic lift coefficient
D	=	aerodynamic drag force, N
d	=	aerodynamic drag deceleration, m/s^2
g	=	gravitational acceleration, m/s^2
h	=	altitude, m
h_s	=	atmospheric scale height, m
h_0	=	reference altitude, m
L	=	aerodynamic lift force, N
L/D	=	lift-to-drag ratio
m	=	vehicle mass, kg
Q_o	=	observability matrix
$\bar{q}$	=	dynamic pressure, kg/m $\cdot$ s^2
R_e	=	equatorial radius, m
r	=	radial distance, m
S	=	aerodynamic surface, m
s	=	downrange, m
t	=	time. s
u	=	input vector
v	=	inertial velocity, m/s
α_0	=	trim angle of attack, rad
γ	=	flight-path angle, rad
λ	=	latitude, rad
θ	=	longitude, rad
μ_M	=	Mars gravitational constant, m^3/s^2
ρ	=	atmospheric density, kg/m^3
ρ_0	=	atmospheric reference density, kg/m^3
ϕ	=	bank angle, rad
ψ	=	azimuth (clockwise from north), rad
$\boldsymbol{\omega}^B$	=	angular rate components in body frame

Received 11 May 2006; revision received 21 September 2006; accepted for publication 25 September 2006.

*Ph.D. Candidate, Department of Electrical Engineering, 2500 Boulevard Université. AIAA Student Member.

†President, NGC Aerospace, 1650 King Ouest, Bureau 202; Professor, Université de Sherbrooke. AIAA Member.

I. Introduction

SEVERAL international space missions scheduled for 2011–2013 have as an objective the return of Mars surface samples to the Earth. Contrary to the Pathfinder [1] and Mars Exploration Rover [2] entry missions, the upcoming missions need to land at precise locations on Mars in order to gather samples of high scientific quality. Therefore, the next generation of landing systems, often-called pinpoint landing systems, will be used to autonomously and safely land on a site selected by scientists. While the Mars Science Laboratory mission (MSL, 2009) is being designed to land within 10 km of the desired landing site, future missions are expected to land within 1 km.

The three most significant sources of landing dispersion at Mars are the following [3]:

1) position and velocity errors at the atmospheric entry point;

2) uncertainties in the atmospheric density and the vehicle aerodynamic characteristics during the hypersonic aerobraking phase;

3) drifts caused by strong winds during the parachute descent phase.

In this scope, terminal landing systems based on lidar navigation are being developed [4] to autonomously find and track a safe site. However, during the atmospheric entry phase, there are no simple solutions for absolute navigation. Optical sensors cannot be used because the vehicle heat shield and plasma sheath impairs them.

Most nonlinear trajectory-tracking methods presented in the literature still assume full state feedback [5–14]. This requires the knowledge of all states at any time. However, unlike on Earth, for Mars missions, it is not trivial to obtain the measurement of all states. Therefore, an observer is required onboard to estimate the system states. The problem arises when only the accelerations and angular rates from an inertial measurement unit (IMU) are available because no altimeter or optical ranging device may be used during the atmospheric hypersonic entry into atmosphere. In this case, the observability analysis shows that some states are unobservable [15,16]. The literature presents only few research works addressing the problem. AutoNav [17,18] from the Deep Space 1 mission or the navigation on the AURORA mission [19] demonstrated interesting

vision-based sensing but, due to the protective aeroshell, this technology cannot be used during the atmospheric entry on Mars. Other work proposed navigation schemes where the two moons of Mars are used as reference ranging beacons. However, this work shows some flaws concerning the range and line of sight with the two moons.

In this context, this paper will discuss the observability of the entry dynamics with the measurement means currently assumed in the literature. Then, innovative solutions will be investigated to overcome the observability problems encountered. Thus, four navigation scenarios will be presented using different radio-ranging measurements from known and unknown references. Finally, the observability of the proposed solutions will be analyzed and validated through simulations.

II. Technical Background

The present contribution offers mainly an improvement to the observability of the atmospheric entry translational dynamics on Mars. Thus, the following research work excludes attitude dynamics and control except for the 6-degrees-of-freedom (DOF) simulations that will be presented later where simple bank angle regulation is implemented as attitude control. In scope of the present contribution on entry navigation, analyses will be of two kinds throughout this section. The first is the analytical characterization of the observability of the states for the translational dynamic models when used in conjunction with a specific measurement set. This kind of analysis is referred to as *observability analysis*. The output models for the measurement sets are referred to as *observation models*.

The second kind of analysis, called *navigation simulation*, is a numerical simulation of the atmospheric entry dynamics where the states are estimated with a nonlinear estimator (Fig. 1). In a navigation simulation, a first simulation run named *true state propagation* is conducted on the real-world software dynamics model in open loop, without estimation, to generate the sensor measurements with the observation models. Thus, this simulation run is simply a discrete propagation of the *true* states through the dynamics from a reference set of true initial conditions. Then, a second simulation run called *onboard state propagation* is also conducted on the same dynamics model in open loop, however, from a different set of initial conditions as known by the internal navigation system. This simulation produces the *propagated* states. Finally, a third simulation run called *state estimation* is conducted (in parallel to the others) on the same entry dynamics but now with the estimator in the loop and from the same estimated initial conditions as for the onboard state propagation simulation above. The results of this state estimation are used to observe the convergence of the *estimated* states compared to the propagated states toward the simulated true states.

Now, the objective of the navigation system is to estimate the vehicle state along its trajectory during atmospheric entry. To clearly understand the research requirements and directions exposed in the next section, the present section analyzes the current techniques for entry navigation on Mars. In the first subsection, the atmospheric entry dynamics model is presented. In the second subsection, the observation models are developed according to the dynamics model of the current sensor technologies. In the third subsection, the observability analysis tools are discussed. Finally, in the two last subsections, the observation models are analyzed and simulated to quantify the observability of their states.

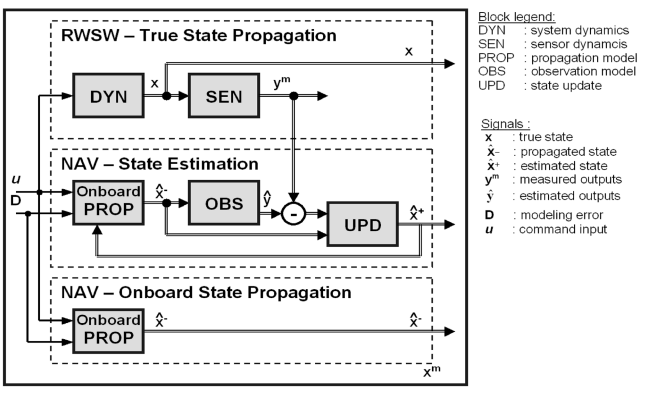

Fig. 1 Navigation simulation scheme.

A. Atmospheric Entry Dynamics

For the sake of simplicity, all the common assumptions for atmospheric entry dynamics used in the literature will be taken here [5,7,10].

1) The planet has a spherical shape,
2) the planet is nonrotating,
3) the atmosphere is steady and nonrotating,
4) the atmospheric density has an exponential behavior,
5) the entry vehicle generates an aerodynamic lift force whose direction and/or magnitude is controllable.

All these assumptions and their relative error contribution on the model have been thoroughly investigated in a related work [16]. A more realistic model will be demonstrated later but for the following demonstrations, a simplified 3-DOF model based on the above assumptions is used to represent the atmospheric entry translational dynamics:

$$\dot{r} = v\sin\gamma \qquad \dot{v} = -d - g(r)\sin\gamma$$
$$\dot{\gamma} = \left(\frac{v}{r} - \frac{g(r)}{v}\right)\cos\gamma + \frac{d}{v}u \qquad \dot{\theta} = \frac{v\cos\gamma\sin\psi}{r\cos\lambda}$$
$$\dot{\lambda} = \frac{v}{r}\cos\gamma\cos\psi \qquad \dot{\psi} = \frac{v}{r}\sin\psi\cos\gamma\tan\lambda + \frac{d}{v\cos\gamma}\frac{\sin\phi}{\cos\phi}u \tag{1}$$

The control input variable u is used to denote the bank angle control:

$$u = \frac{L}{D}\cos\phi \tag{2}$$

Then, d is given by

$$d = B\bar{q} \tag{3}$$

where the aerodynamic pressure $\bar{q}$ and B are

$$\bar{q} = \tfrac{1}{2}\rho v^2 \tag{4}$$

$$B = \frac{C_D S}{m} \tag{5}$$

Finally, the atmospheric density is approximated by the conventional exponential model

$$\rho = \rho_0 \exp\left(\frac{r_0 - r}{h_s}\right) \tag{6}$$

where $\rho_0 = 2e-4\ \text{kg/m}^3$ is the reference density, $r_0 = 3,437,200$ m is the reference radial position (40 km above surface), and $h_s = 7500$ m is the atmospheric scale height.

The subspace described by the first three equations of the 3-dimensional model Eq. (1) is defined in the literature [16] as the longitudinal dynamics. This dynamics is often augmented with the knowledge of the longitudinal position or downrange s to form the following set of equations:

$$\dot{r} = v\sin\gamma \qquad \dot{v} = -d - g(r)\sin\gamma$$
$$\dot{\gamma} = \left(\frac{v}{r} - \frac{g(r)}{v}\right)\cos\gamma + \frac{d}{v}u \qquad \dot{s} = v\cos\gamma \tag{7}$$

B. Observation Models

The sensor measurements are used to construct the outputs of the observation models. For the onboard software, these models are

equivalent to the sensor models and are used on one hand to generate the measurement outputs for the true state dynamics simulations, and on the other hand inside the estimator correction algorithm (state update) for the estimation simulations. There are limitations concerning the type of sensor measurements available during the atmospheric entry. The general navigation scenario assumed in the literature is based on IMU measurements alone (accelerometers and rate gyroscopes). This is referred to as the *default navigation scenario* in the remainder of this document because it relies on basic principles used in conventional entry dynamics and control. It constitutes also the reference scenario for future performance comparisons. The following observation models are developed based on IMU measurements and associated with the models of the system dynamics presented previously.

1. Longitudinal Observation Model

The longitudinal observation model is based on the simplified longitudinal dynamics Eq. (7). In the longitudinal plane, the measurements are the drag and lift acceleration, and the angular rate around the y axis [approximated here by the flight-path angle (FPA) rate]. Therefore, with the aerodynamics simplifications of the longitudinal model, the measurement output vector is

$$\mathbf{y} = \begin{bmatrix} d \\ dL/D \\ \dot{\gamma} \end{bmatrix} \tag{8}$$

where d is calculated with Eq. (3) and $\dot{\gamma}$ with the state equation of the model.

2. Three-DOF Observation Model

The design model was defined previously with the simplified 3-DOF dynamics Eq. (1) and state vector:

$$\mathbf{x} = [\, r \quad v \quad \gamma \quad \psi \quad \theta \quad \lambda \,]^T \tag{9}$$

For this model, the IMU provides the system with the three components of the acceleration **a**:

$$\mathbf{y} = [\mathbf{a}] \tag{10}$$

where the output equation is defined as

$$\mathbf{y} = \begin{bmatrix} -d \\ 0 \\ -dL/D \end{bmatrix} \tag{11}$$

C. Simulation Input Command

In navigation simulations, there is no need for guidance and control of the trajectory because only the state estimation performance is looked at. Therefore, all simulations are conducted in open loop with respect to the trajectory control such that the lander follows more or less an unguided trajectory profile. Thus, the vehicle keeps its reference trim angle but the produced lift vector remains uncontrolled.

For 3-DOF navigation simulation purposes, the initial command input to the system dynamics Eq. (1) is set for a constant bank angle $\phi = \pi/4$. Unless otherwise noticed, all the navigation simulations in this paper will be initialized with these conditions.

D. Observability Analysis for the Default Navigation Scenario

For an estimator to converge, all the states used in the observation model must be observable, in which case complete observability of the system is obtained. If one or more states cannot be observed through the available measurements, only partial observability of the system is obtained. In this case, some states may diverge during estimation and the estimator may become unstable. Because of the nonlinearity and instability of the system, the tools that will be used throughout this paper for analyses are the observability matrix and the Jordan canonical form (JCF) [20] also presented in the Appendix. Following are preliminary observability analyses for the atmospheric entry dynamics using IMU measurements alone.

1. Observability of the Longitudinal Model

To conduct a preliminary analysis, a state-space representation of the longitudinal dynamics is developed through linearization of the nonlinear dynamics. Now, to test the system with the observability matrix, the dynamics must first be linearized about the operation point. Thus, for the longitudinal dynamics Eq. (7) and the observation model Eq. (8), partial derivatives give the following linearized state-space system with respect to the state variations Δr, Δv, $\Delta\gamma$, and Δs:

$$\begin{bmatrix} \Delta\dot{r} \\ \Delta\dot{v} \\ \Delta\dot{\gamma} \\ \Delta\dot{s} \end{bmatrix} = \begin{bmatrix} 0 & \sin\gamma & v\cos\gamma & 0 \\ \frac{d}{h_s} + \frac{2g}{r}\sin\gamma & -\frac{2d}{v} & -g\cos\gamma & 0 \\ \left(\frac{2g}{vr} - \frac{v}{r^2}\right)\cos\gamma - \frac{d}{h_s v}u & \left(\frac{1}{r} + \frac{g}{v^2 r}\right)\cos\gamma + \frac{d}{v^2}u & \left(\frac{g}{v} - \frac{v}{r}\right)\sin\gamma & 0 \\ 0 & \cos\gamma & -v\sin\gamma & 0 \end{bmatrix} \begin{bmatrix} \Delta r \\ \Delta v \\ \Delta\gamma \\ \Delta s \end{bmatrix} + \begin{bmatrix} 0 \\ 0 \\ \frac{d}{v} \\ 0 \end{bmatrix} \Delta u \tag{12}$$

$$\begin{bmatrix} \Delta d \\ \Delta dL/D \\ \Delta\dot{\gamma} \end{bmatrix} = \begin{bmatrix} -\frac{d}{h_s} & \frac{2d}{v} & 0 & 0 \\ -\frac{d}{h_s}L/D & \frac{2d}{v}L/D & 0 & 0 \\ \left(\frac{2g}{vr} - \frac{v}{r^2}\right)\cos\gamma - \frac{d}{h_s v}u & \left(\frac{1}{r} + \frac{g}{v^2 r}\right)\cos\gamma + \frac{d}{v^2}u & \left(\frac{g}{v} - \frac{v}{r}\right)\sin\gamma & 0 \end{bmatrix} \begin{bmatrix} \Delta r \\ \Delta v \\ \Delta\gamma \\ \Delta s \end{bmatrix} + \begin{bmatrix} 0 \\ 0 \\ \frac{d}{v} \end{bmatrix} \Delta u \tag{13}$$

These matrices are computed for different operation points along the trajectory. In each case, the observability matrix has a rank of 3 for $\gamma \neq 0$ and $\gamma \neq \pi$. This means that, since the system has a rank of 4, there is one unobservable state. A reduced state set may reveal which one is unobservable. Let us remove the downrange dynamics (this can be done because the dynamics equations do not explicitly depend on downrange). For the reduced linearized state-space model, the observability matrix has also a rank of 3 at any linearization point along the trajectory. Note that the observability analysis assumes known reference atmospheric density and

aerodynamic parameters. An analysis with the output matrix of the JCF transformation for this system will confirm that all three states are reasonably observable through the accelerometer measurements alone. Hence, the reduced longitudinal dynamics (r, v, g) are completely observable whereas the actual horizontal position (downrange s) of the vehicle cannot be estimated from the IMU measurements alone. Intuitively, this could have been expected because only accelerations and rates are measured and no springlike dynamics binds the downrange to the measurements. In terms of eigenvalues, the downrange dynamics places a new pole at the origin (zero), which corresponds to a pure integrator. In other words, the actual position across the surface of the planet cannot be estimated without the knowledge of its initial conditions and with an acceleration measurement in this longitudinal direction (the projection of the two accelerometers). This is not the case for the vertical position (altitude) because the atmospheric density brings a relation between the altitude and the vertical acceleration that makes the state observable.

2. *Observability of the Three-DOF Model*

The observability analysis procedure used for the longitudinal dynamics was automated with a software tool (MATLAB) for the 3-DOF model Eq. (1). From the longitudinal state-space model above, it can be seen that there is a redundant measurement because the second output equation is a linear combination of the first when L/D is considered known. Therefore, the second output is not useful in the system description and removing it does not change the observability of the system. However, instead of removing this redundant measurement equation, we could use it to observe the L/D parameter along with the other states. Thus, adding this L/D parameter to the state vector yields the augmented set:

$$\mathbf{x} = [r \quad v \quad \gamma \quad \psi \quad \theta \quad \lambda \quad L/D]^T \tag{14}$$

In this case, the L/D parameter is assumed nearly constant and the associated differential equation is

$$\frac{dL/D}{dt} = 0 \tag{15}$$

while other 3-DOF state equations remain unchanged. Then, the linear state-space model is derived from Eqs. (1) and (15) and computed about different linearization points of the entry trajectory. The added reference L/D parameter is linearized by differentiation of Eq. (15) with respect to the state vector Eq. (14):

$$\Delta(\dot{L/D}) = \frac{\partial(\dot{L/D})}{\partial \mathbf{x}}\Delta\mathbf{x} + \frac{\partial(\dot{L/D})}{\partial \mathbf{u}}\Delta\mathbf{u} = 0 \tag{16}$$

The output measurements are formed with the 3-axis acceleration and 3-axis angular rate from the IMU (default navigation scenario).

For this default navigation scenario, the observability matrix reveals that this 3-DOF system of dimension 7 has now three unobservable states over the entire trajectory. By extrapolation from the previous observations on the longitudinal model, these unobservable states are expected to belong to the horizontal position dynamics: the longitude, the latitude, and the azimuth.

E. Navigation Simulations for the Default Navigation Scenario

To validate the assumptions in the above observability analysis, 3-DOF and 6-DOF navigation simulations are conducted on the nonlinear model for the IMU measurement outputs. The 3-DOF simulation uses the simplified translational model Eq. (1) and observation model Eq. (10) presented earlier. In counterpart, the 6-DOF simulation is based on a complete translational and rotational model free from the modeling simplifications introduced earlier. This model is not presented here for sake of simplicity but is available in a related publication [16].

Both simulation types use the unscented Kalman filter (UKF) [21,22] because this estimator is better suited for nonlinear models. Several versions of the filter were implemented as comparison for both state and parameter estimation: the simplex UKF [23], the scaled UKF [24], the square-root UKF [25,26], and the second-order simplex UKF [27]. All estimator versions produced similar results and only the scaled UKF is kept for the analysis throughout this document. The tuning parameters used for that particular filter are scales $\alpha = 0.6, \beta = 2$, and $\kappa = 3 - n$, where n is the state dimension. The filter is clocked at 50 Hz in phase with the measurements.

The entry conditions for the real-world software (true state propagation) are set with an initial altitude of 125 km, velocity of 6900 m/s, flight-path angle of −12 deg, azimuth 89 deg, and longitude and latitude at the origin. The UKF estimator is initialized with different entry states than the real-world software with an altitude error of 1 km, velocity error of 100 m/s, 1 deg of both azimuth and FPA error, and finally, 0.02 deg of longitude and latitude angle errors. In the case of 6-DOF simulations, as explained before, the quaternions are only propagated (integrated) from rate measurements. To limit the impact of the attitude error on the estimation of the other states, the quaternions are initially set equal for both the true state propagation and the state estimation. As for the angular rates, they are initially set to zero. All states are assumed Gaussian distributed.

Furthermore, to translate the entry dispersion causes to the simulations, the estimator uses the real-world software entry dynamics but with some modeling errors. Thus, an arbitrary 10% modeling error is implemented for the following parameters: the reference atmospheric density, the ballistic coefficient, and the L/D ratio. The simulation conditions and parameters are summarized in Table 1.

The simulation is terminated at the end of the atmospheric entry phase at 10 km altitude (roughly after 400 s of simulation) where the hypersonic chute is deployed. The results of the 3-DOF and 6-DOF navigation simulations are presented in the two subsections below.

1. *Three-DOF Simulation Results*

The results of the 3-DOF navigation simulation presented in Fig. 2 show 14 subplots. The upper-row plots represent the evolution of the six translational dynamics states Eq. (14) and the identified L/D parameter. One remark is that the first state r has been replaced with an equivalent altitude h from a flat surface. This postprocessed representation does not, however, affect the simulation performance and is just used for convenience. On each subplot, the three curves represent the true, propagated, and estimated states, respectively. On the lower-row plots, the above propagated and estimated states are compared to the true states and the errors are shown along with the estimated standard deviations. As can been seen, the estimation errors for all the estimated states are much lower than for the propagated states after 50 s of simulations (after the dynamic pressure has built up). Therefore, the results clearly show that, compared to the onboard state propagation only, the state estimation using IMU measurements can achieve a much better knowledge of the current state. Furthermore, the results show that the estimation of the L/D parameter can be achieved as expected from the observability analysis. However, with the IMU navigation, some estimated states still do not converge such as the latitude, while other states keep a relative constant error with the true states such as the

Table 1 Initial conditions and parameters for navigation simulations

	True	Estimated
Initial altitude h_0	125 km	126 km
Initial velocity v_0	6900 m/s	6910 m/s
Initial flight path γ_0	−12 deg	−13 deg
Initial azimuth ψ_0	89 deg	90 deg
Initial longitude θ_0	0.00 deg	0.02 deg
Initial latitude λ_0	1.00 deg	1.02 deg
Initial rate $\boldsymbol{\omega}_0^B$	0 rad/s	0 rad/s
Initial quaternions	[−0.57, −0.70, 0.33, 0.27]	Same
Ballistic coefficient B	0.016 m^2/kg	0.0176 m^2/kg
L/D ratio	0.156	0.172
Reference density ρ_0	2.0×10^{-4} kg/m^3	2.2×10^{-4} kg/m^3

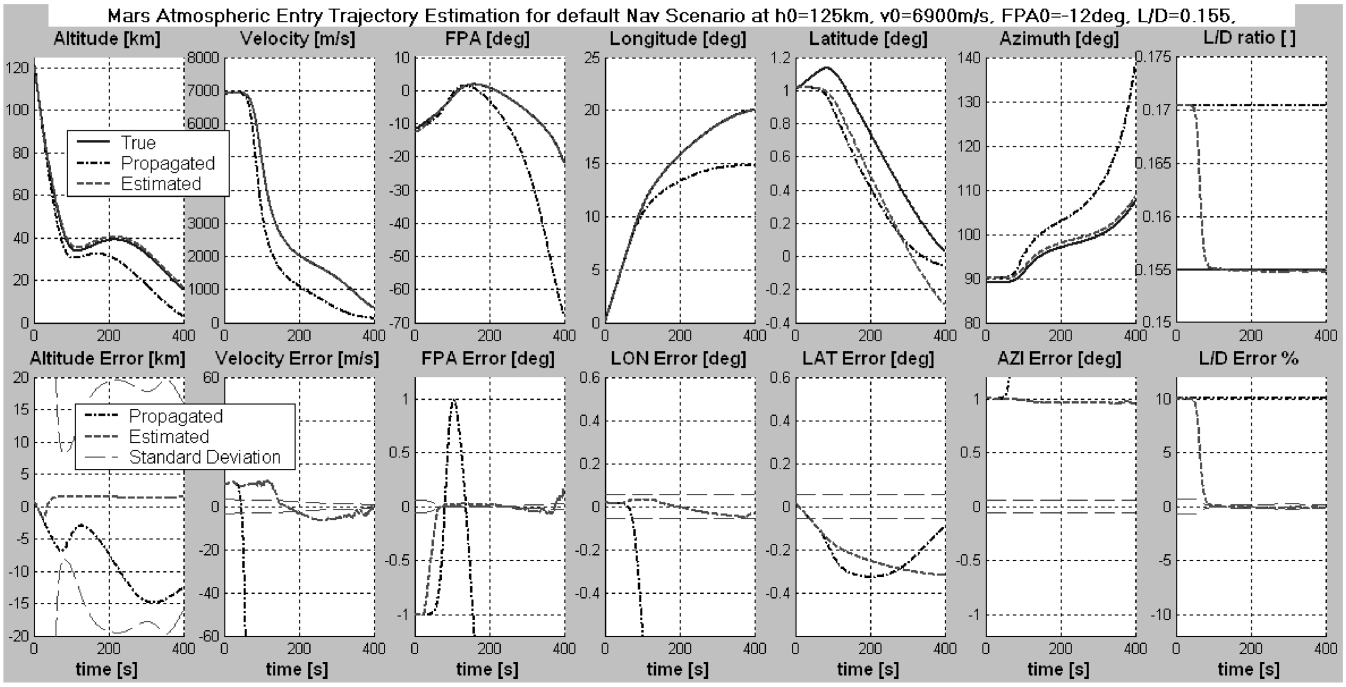

Fig. 2 State estimation of the 3-DOF atmospheric entry dynamics using the default IMU-based navigation scenario for a vehicle with $L/D = 0.155$, $B = 0.016\ \mathrm{m^2/kg}$.

altitude and the azimuth. This corroborates with the observability analysis in the sense that the system is not completely observable with IMU measurements alone. In this case of partial observability, the use of state estimators is still useful though because some states may accurately be estimated. Thus, the corridor of the estimated trajectories still gets closer to the expected trajectory than when no states are estimated at all in the case of onboard state propagation because the dispersions are reduced by the addition of IMU measurements (Fig. 3).

2. Six-DOF Simulation Results

The results of the 6-DOF navigation simulation presented in Fig. 4 demonstrates similar performance as for the 3-DOF simulation: improvement in the estimation of all the states but the asymptotical convergence is not achieved for some states. However, the simulation shows that the L/D parameter is still estimated accurately.

III. Innovative Observability Solution

Although the default scenario using IMU measurements may show interesting performance for navigation compared to onboard state propagation, the divergence from some states could not ensure stability of the filter, and this may not be acceptable in the present context of precision landing. Therefore, new navigation techniques must be developed in order to obtain complete observability and estimation accuracy during atmospheric entry and achieve the precision landing required in future missions.

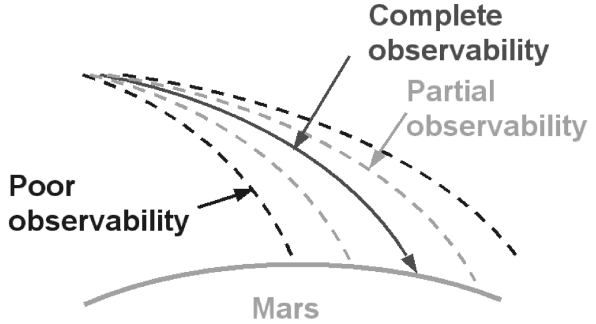

Fig. 3 Estimated trajectory corridor with increased system observability.

An innovative solution, which has not been very exploited in the literature, for atmospheric entry on Mars is to make use of the radio communications as sensor measurements. A first draft of such a system is being investigated for the MSL mission [28,29]. Two possible measurements are available: range and relative velocity. The range measurement can achieve centimeter accuracy using global positioning system (GPS) technology receivers modified for Mars applications [30], whereas the relative velocity measurement is based on conventional Doppler radio.

This sensor concept, coupled to the IMU measurements, leads to a wide variety of navigation schemes to achieve the precision landing mission objectives. These schemes are the subjects of the second major contribution of this research project: four new navigation scenarios that augment the observability of the entry dynamics. The scenarios are developed and analyzed in the following four sections of this paper. But first, the radio blackout issue during atmospheric entry is discussed.

To protect the components from the excessive heat during atmospheric entry, the vehicle is equipped with a *heat shield*, also called *aeroshell*, hindering optical and line-of-sight measurements toward the direction of motion. Furthermore, a layer of plasma forms around the vehicle resulting from ionization of the atmospheric gases as they are compressed and heated by the hypersonic shock (Fig. 5). This plasma sheath blocks low frequency radio signals during some portion of the descent at about 60 km and may render radio-based navigation difficult during that period.

A thorough analysis is conducted by Morabito [31] to determine the impact of the sheath of ionized particles on radio transmissions at different frequencies. It is demonstrated that this plasma sheath did not block the high frequency communication used for the Mars Exploration Rover (MER) mission during its entry in the Martian atmosphere. It is assumed likewise for radio ranging throughout this paper.

IV. Navigation Scenario 1

The first navigation scenario analyzed consists of adding one radio-ranging measurement to the default IMU-based navigation. In the following, this proposed navigation scenario 1 is represented

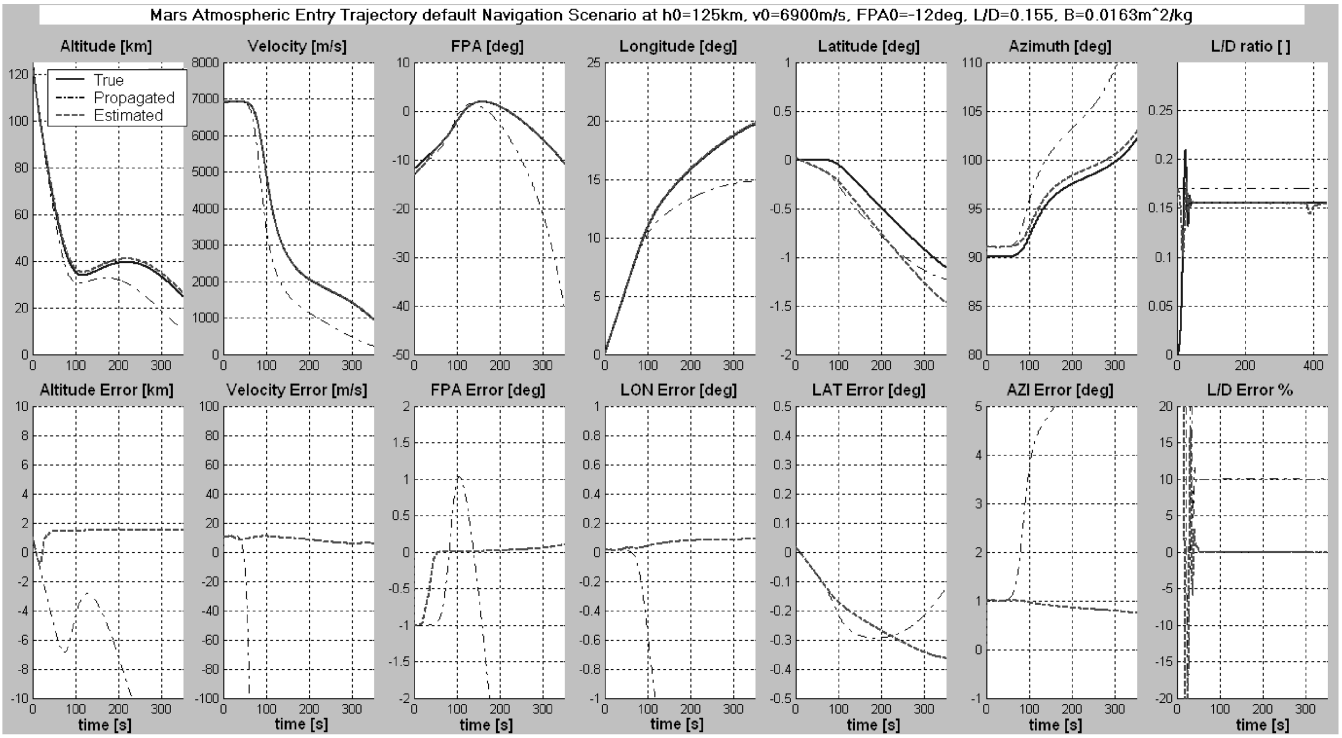

Fig. 4 State estimation of the 6-DOF atmospheric entry dynamics using the default IMU-based navigation scenario for a vehicle with $L/D = 0.155$, $B = 0.016\ \mathrm{m^2/kg}$.

with an observation model. Then the model is tested with the observability matrix. Finally, navigation simulations are conducted on this scenario model to validate the observability analysis.

A. Observation Model

The obvious approach to use radio ranging for navigation relies on known references. Thus, two possible one-way radio beacon sources called *reference beacon* have been identified in Fig. 6 for navigation scenario 1.

The first source is an orbiter spacecraft called the *Orbiter*, which may be either already in orbit around Mars or part of a sample-return mission, for instance. The second source is a fixed beacon on the planet surface installed from a previous mission (Fig. 6b). For both type of sources, the inertial position of the reference beacon is well known to the lander (from updated trajectory propagation data through the beacon signal, for instance).

Now, the relative position vector between the lander and the orbiter is defined as

$$\mathbf{R}_{\text{Beacon}} = \mathbf{r}_{\text{Lander}} - \mathbf{r}_{\text{Beacon}} \tag{17}$$

and, the range is given by its norm

$$R = |\mathbf{R}| = \sqrt{\mathbf{R}_x^2 + \mathbf{R}_y^2 + \mathbf{R}_z^2} \tag{18}$$

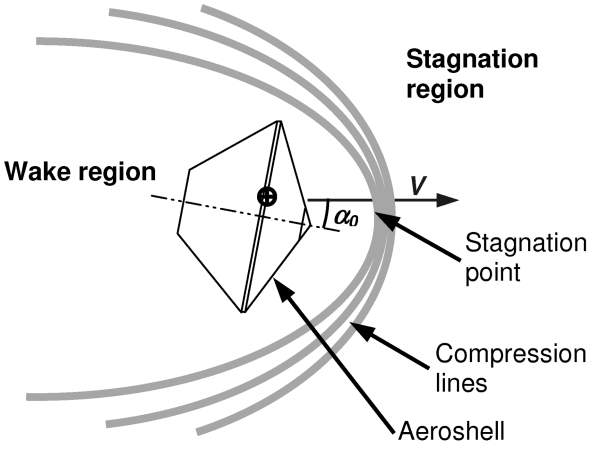

Fig. 5 Plasma sheath of ionized particles during atmospheric entry.

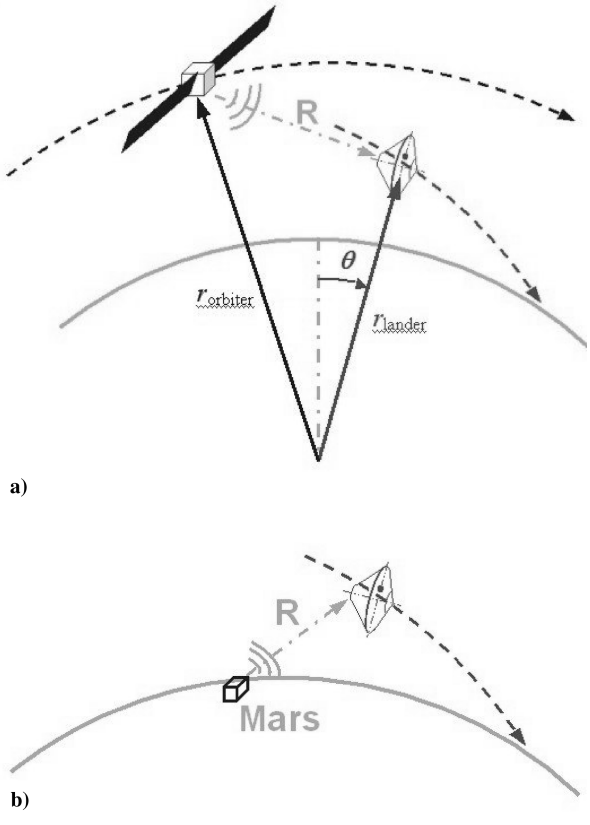

Fig. 6 Radio-ranging measurement from two known beacon sources.

Then, the position vector of the lander is

$$\boldsymbol{r}_{\text{Lander}} = r \begin{bmatrix} \cos\lambda\cos\theta \\ \cos\lambda\sin\theta \\ \sin\lambda \end{bmatrix} \tag{19}$$

Because the lander knows the inertial position $\mathbf{r}_{\text{Beacon}}$ of the reference beacon at any time, the radio-ranging measurement R brings the position of the lander (either downrange or longitude θ) in relation with its radial location r (Fig. 6a) such that this added measurement dynamics would increase the observability of the lander position by one rank. Now, the navigation system for this scenario requires the same 3-DOF entry dynamics Eqs. (1) and (15) as for the default navigation scenario using IMU only. However, the radio ranging provides the system with the range measurement R from the reference beacon. Thus, in addition to the IMU measurements, the observation outputs for this 3-DOF model become

$$\mathbf{y} = \begin{bmatrix} \mathbf{a}^B \\ R \end{bmatrix} \tag{20}$$

B. Observability Analysis

An automated analysis similar to the one presented previously is conducted on the augmented observation model for navigation scenario 1. The results are presented here.

First, the added range measurement output is linearized by differentiation of Eq. (18) with respect to the state vector Eq. (14):

$$\begin{aligned} \Delta R &= \frac{\partial R}{\partial \mathbf{x}}\Delta\mathbf{x} + \frac{\partial R}{\partial \mathbf{u}}\Delta\mathbf{u} = \frac{1}{R}\left(\mathbf{R}_1\frac{\partial \mathbf{R}_1}{\partial \mathbf{x}} + \mathbf{R}_2\frac{\partial \mathbf{R}_2}{\partial \mathbf{x}} + \mathbf{R}_3\frac{\partial \mathbf{R}_3}{\partial \mathbf{x}}\right) \\ &= \frac{1}{R}\left(\mathbf{R}_1\begin{bmatrix} \cos\lambda\cos\theta\Delta r \\ 0 \\ 0 \\ 0 \\ -r\cos\lambda\sin\theta\Delta\theta \\ -r\sin\lambda\cos\theta\Delta\lambda \\ 0 \end{bmatrix} + \mathbf{R}_2\begin{bmatrix} \cos\lambda\sin\theta\Delta r \\ 0 \\ 0 \\ 0 \\ r\cos\lambda\cos\theta\Delta\theta \\ -r\sin\lambda\sin\theta\Delta\lambda \\ 0 \end{bmatrix} + \mathbf{R}_3\begin{bmatrix} \sin\lambda\Delta r \\ 0 \\ 0 \\ 0 \\ 0 \\ r\cos\lambda\Delta\lambda \\ 0 \end{bmatrix}\right) \end{aligned} \tag{21}$$

Then, this linear dynamics is added to the previous linear observation model and the observability matrix is computed at different points along the trajectory.

The analysis shows that the observability matrix of the linearized system is full rank at any points along the trajectory, given $-90 < \lambda < 90$ deg. Therefore, the linear lander dynamics should become completely observable at any point of the trajectory by the addition of a single range measurement from a reference beacon to the default IMU-based navigation scenario. However, this analysis does not indicate if some of the states are only barely observable. Thus, the analysis is pushed a little further by transforming the linear system into the Jordan canonical form. A sample transformation at the end of the entry trajectory ($t = 350$ s) results in the following transformed output matrix:

$$\bar{\mathbf{C}} = \begin{bmatrix} 0 & 21.95 & 21.22 & 0 & 3.43 & 3.43 & 0 \\ 0 & 0 & 0 & 0 & 0 & 0 & 0 \\ 0 & 5.52 & 0.44 & 0 & 0.071 & 0.071 & 0 \\ 2121 & 9.97\times10^8 & 6.93\times10^6 & 3.36\times10^8 & 1308 & 1308 & 3.36\times10^8 \end{bmatrix}$$

In this matrix, it can be seen that the first column (associated with the first transformed state) does not hold any significant value compared to the other columns (2121 compared to 10×10^8). Therefore, the associated state is only barely observable through the added range output (last row). Furthermore, the fifth and sixth columns contain relatively small numbers on the first row compared to the second and third columns. Hence, this analysis demonstrates partial observability of the system and this will be tested further with the following navigation simulation.

C. Navigation Simulations

A navigation simulation is conducted on the 3-DOF model of navigation scenario 1 with the state vector given as Eq. (14). As before, the simulation assumes the initialization of the state estimator with the values of Table 1 and the 10% modeling error on the atmospheric density and aerodynamic coefficients of the entry. Concerning the reference beacon, this simulation assumes a fixed beacon on the planet surface at the origin ($\theta = 0$ deg, $\lambda = 0$ deg).

The 3-DOF simulation results for navigation scenario 1 are presented in Fig. 7 in the same fashion as previously for the default navigation scenario. However, instead of displaying the propagated state, the default IMU navigation scenario results are used in comparison to observe directly the improvement when adding a range measurement. The results show that the L/D ratio is still estimated accurately with the new navigation scenario 1 as for the default navigation scenario. This occurs after the dynamic pressure has built up ($t > 50$ s) because before, the observability of the aerodynamics was very weak. However, the estimated states for navigation scenario 1 show roughly the same accuracy than for the default navigation scenario using IMU measurements only since the state errors on the graph are similar. The estimated longitude and latitude still diverge from the true state. Therefore, the nonlinear system is not completely observable although the linear observability matrix on navigation scenario 1 indicates otherwise. Obviously, as detected with the JCF, the state that is barely observable did not make the estimation converge and cope with the 10% parametric error introduced in the estimator model on both the atmospheric density and ballistic parameter.

Navigation simulations on the 6-DOF model are not presented here for sake of simplicity but they demonstrate similar results. The only gain that could be expected is that the addition of the range

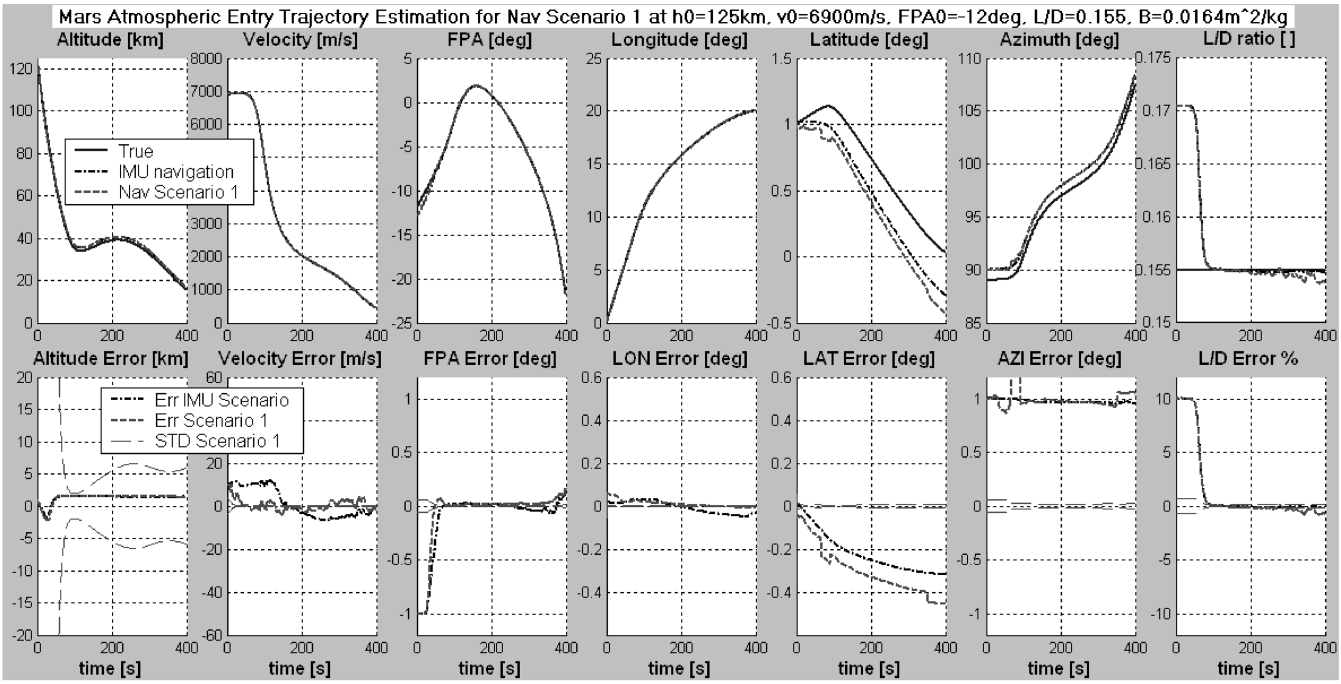

Fig. 7 State estimation comparison between IMU navigation and navigation scenario 1 with a 3-DOF atmospheric entry simulation for a vehicle with $L/D = 0.155$, $B = 0.016\ \mathrm{m^2/kg}$.

measurement might contribute to reduce the error propagation of the nonobservable states through the estimation filter.

D. Contribution Summary

In summary, in addition to the IMU measurements, navigation scenario 1 uses one radio ranging from a reference beacon. This augmented system improves only slightly the estimation accuracy compared to the default IMU-based navigation scenario. However, the L/D ratio of the entry vehicle is accurately estimated along with some states.

V. Navigation Scenario 2

The second navigation scenario analyzed consists of adding a second radio-ranging measurement to the previous navigation scenario 1 to improve further the observability. Similar to the previous scenario, this proposed navigation scenario 2 is represented with an observation model. Then the model is tested with the observability matrix. Finally, simulations are conducted on this scenario model to validate the observability analysis.

A. Observation Model

As demonstrated for navigation scenario 1, some states are not estimated accurately on the nonlinear models with one range measurement, although the observability analysis on the linear system showed complete observability. Therefore, more measurements are required to improve the estimator performance.

The next step for enhancing the radio-ranging navigation is to use two known reference beacons (either orbiters or on the planet surface) instead of a single one in the case of the previous scenario. Thus, in addition to the IMU measurements, two ranges R_{Beacon1} and R_{Beacon2} are identified for navigation scenario 2:

$$\mathbf{R}_{\mathrm{Beacon1}} = \mathbf{r}_{\mathrm{Lander}} - \mathbf{r}_{\mathrm{Beacon1}} \qquad \mathbf{R}_{\mathrm{Beacon2}} = \mathbf{r}_{\mathrm{Lander}} - \mathbf{r}_{\mathrm{Beacon2}} \tag{22}$$

where $\mathbf{r}_{\mathrm{Beacon1}}$ and $\mathbf{r}_{\mathrm{Beacon2}}$ are the known inertial positions of the two reference beacons.

Now, the model of the dynamics for this scenario remains the same as for the default navigation using IMU only. However, the dual radio ranging provides the system with the range from two distinct references. Thus, in addition to the IMU measurements, the observation outputs for the 3-DOF model become

$$\mathbf{y} = \begin{bmatrix} \mathbf{a}^B \\ R_{\mathrm{Beacon1}} \\ R_{\mathrm{Beacon2}} \end{bmatrix} \tag{23}$$

B. Observability Analysis

The same automated analysis as before is conducted on the augmented 3-DOF observation model for navigation scenario 2. The results are presented here below. The added range outputs are linearized by differentiation with Eq. (21) as for navigation scenario 1.

As usual, this linear dynamics is added to the previous linear observation model and the observability matrix is computed at different points along the trajectory. For this scenario, the observability analysis shows that the observability matrix of the linearized system is full rank at any linearization points along the trajectory, given $-90 < \lambda < 90$ deg. Obviously, the linear lander dynamics is still completely observable at any point of the trajectory by the addition of a second range measurement from a reference beacon. However, a sample transformation of the linearized system into the JCF at $t = 350$ s results in the following transformed output matrix:

$$\bar{\mathbf{C}} = \begin{bmatrix} 0 & 21.95 & 21.22 & 0 & 3.43 & 3.43 & 0 \\ 0 & 0 & 0 & 0 & 0 & 0 & 0 \\ 0 & 5.52 & 0.44 & 0 & 0.071 & 0.071 & 0 \\ 2121 & 9.97 \times 10^8 & 6.93 \times 10^6 & 3.36 \times 10^8 & 1308 & 1308 & 3.36 \times 10^8 \\ 2199 & 9.15 \times 10^9 & 1.07 \times 10^7 & 7.24 \times 10^8 & 1116 & 1116 & 7.24 \times 10^8 \end{bmatrix}$$

Similar to navigation scenario 1, the first column (associated with the first transformed state) does not hold any significant value compared to the other columns. Therefore, the associated state is only barely observable through the added two range outputs (last two rows). This time, however, the estimator performance on the other states might be significantly improved by the addition of this second measurement. This is demonstrated through the following navigation simulation.

C. Navigation Simulations

Similar to navigation scenario 1, a navigation simulation is conducted on the 3-DOF observation model of navigation scenario 2 to validate the observability analysis. As before, the simulation assumes the initialization of the state estimator with the values of Table 1 and the 10% modeling error on the atmospheric density and aerodynamic coefficients of the entry. Concerning the reference beacons, this simulation assumes a second fixed beacon on the planet surface at $\theta = 5.7$ deg, $\lambda = 5.7$ deg (about 475 km from the first reference beacon).

The 3-DOF simulation results for navigation scenario 2 are presented in Fig. 8 in the same fashion as previously given for navigation scenario 1. The plots show that the L/D ratio is estimated accurately after the dynamic pressure has built up ($t > 50$ s). Furthermore, the estimated position states (longitude and latitude) are much closer to the true states than for navigation scenario 1. This clearly demonstrates that navigation scenario 2 using a second range measurement has an improved observability. This performance might be sufficient for some precision landing missions because the remaining 0.004 deg constant error on the longitude estimate corresponds to about 250 m range on the planet surface.

Finally, it should be remembered that two dynamic parameters (atmospheric reference density and ballistic coefficient) are set with 10% error between the true state propagation and the state estimation models on all navigation simulations up to now. This constant parametric error might be at the source of the residual constant error on the altitude and longitude estimates. This will be investigated further in the next navigation scenario.

D. Contribution Summary

In summary, in addition to the IMU measurements, navigation scenario 2 proposes two ranging measurements from known reference beacons to improve the observability of the system. This is assessed through observability analyses and navigation simulations. It is observed that the estimator modeling errors still degrade the estimation accuracy.

VI. Navigation Scenario 3

As demonstrated for navigation scenario 2, all translational states are estimated with sufficient accuracy on the nonlinear models with the IMU and two range measurements. The next step for radio-ranging navigation is the use of three known reference beacons as used in the previous scenarios. The assumption is that some parameters of the atmospheric entry models might be observed through this third range measurement. As explained earlier, one of the most uncertain models is the atmospheric density. Therefore, the third navigation scenario analyzed consists of adding a third radio-ranging measurement to the previous navigation scenario 2 to estimate an atmospheric reference density parameter. For this proposed navigation scenario 3, the observation model is developed, then analyzed with the observability matrix, and finally simulated.

A. Observation Model

The reference density parameter ρ_0 from the exponential model Eq. (6) was arbitrarily chosen in this navigation scenario 3 to be estimated along with the other system states. Thus, the augmented state vector for the 3-DOF entry dynamics is

$$\mathbf{x} = [\, r \quad v \quad \gamma \quad \psi \quad \theta \quad \lambda \quad L/D \quad \rho_0 \,]^T \tag{24}$$

with the following parameter state dynamics:

$$\frac{d\rho_0}{dt} = 0 \tag{25}$$

while the other state equations remain unchanged from the default navigation scenario.

Now, the triple radio ranging provides the system with range from three distinct reference beacons. Thus, in addition to the IMU measurements, the observation outputs for the 3-DOF model become

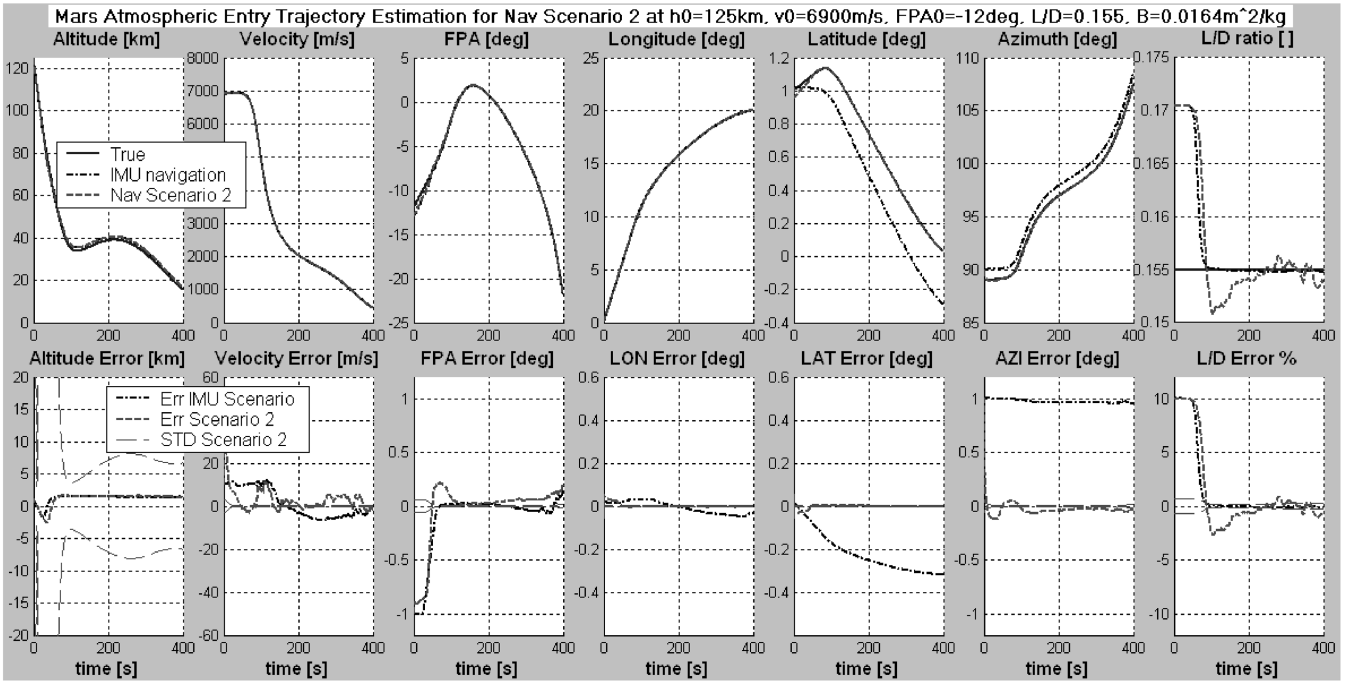

Fig. 8 State estimation comparison between IMU navigation and navigation scenario 2 with a 3-DOF atmospheric entry simulation for a vehicle with $L/D = 0.155$, $B = 0.016$ m^2/kg.

$$\mathbf{y} = \begin{bmatrix} \mathbf{a}^B \\ R_{\text{Beacon1}} \\ R_{\text{Beacon2}} \\ R_{\text{Beacon3}} \end{bmatrix} \tag{26}$$

where the associated range vectors are given by

$$\mathbf{R}_{\text{Beacon1}} = \mathbf{r}_{\text{Lander}} - \mathbf{r}_{\text{Beacon1}} \qquad \mathbf{R}_{\text{Beacon2}} = \mathbf{r}_{\text{Lander}} - \mathbf{r}_{\text{Beacon2}}$$
$$\mathbf{R}_{\text{Beacon3}} = \mathbf{r}_{\text{Lander}} - \mathbf{r}_{\text{Beacon3}} \tag{27}$$

where $\mathbf{r}_{\text{Beacon1}}$, $\mathbf{r}_{\text{Beacon2}}$, and $\mathbf{r}_{\text{Beacon3}}$ are the known inertial positions of the three reference beacons.

B. Observability Analysis

The same automated analysis as before is conducted on the augmented 3-DOF observation model for navigation scenario 3. The results are presented here. The added range outputs are linearized by differentiation with Eq. (21) as for navigation scenario 1. The added reference density state is linearized by differentiation of Eq. (25) with respect to the augmented state vector Eq. (24) with

$$\Delta\dot{\rho}_0 = \frac{\partial\dot{\rho}_0}{\partial\mathbf{x}}\Delta\mathbf{x} + \frac{\partial\dot{\rho}_0}{\partial\mathbf{u}}\Delta\mathbf{u} = 0 \tag{28}$$

As usual, this linear dynamics is added to the previous linear observation model and the observability matrix is computed at different points along the trajectory. For this scenario, the observability analysis shows that the observability matrix of this linearized system augmented with the reference density parameter remains full rank at any linearization points along the trajectory. Hence, with the addition of the third range output to navigation scenario 2, both the system translational dynamics and the reference density are expected to be completely observable along the entire trajectory. However, a sample transformation of the linearized system into the JCF at $t = 350$ s results in the following transformed output matrix:

$$\bar{\mathbf{C}} = \begin{bmatrix} 0 & 126 & 21.2 & 0 & 3.43 & 3.43 & 0 & 149 \\ 0 & 0 & 0 & 0 & 0 & 0 & 0 & 0 \\ 0 & 128 & 0.44 & 0 & 0.071 & 0.071 & 0 & 134 \\ 2122 & 7.87\times10^{9} & 6.93\times10^{6} & 3.36\times10^{8} & 1308 & 1308 & 3.36\times10^{8} & 8.87\times10^{9} \\ 2199 & 1.70\times10^{10} & 1.07\times10^{7} & 7.24\times10^{8} & 1116 & 1116 & 7.24\times10^{8} & 1.91\times10^{10} \\ 2277 & 2.93\times10^{10} & 1.57\times10^{7} & 1.25\times10^{9} & 1121 & 1121 & 1.25\times10^{9} & 3.31\times10^{10} \end{bmatrix}$$

It can be seen that the added reference density parameter in the transformed state vector (somewhat included in the last column of the matrix) is observable through the range measurements. However, similar to the previous navigation scenarios, the first column (associated with the first transformed state) does not hold any significant value compared to the other columns. Therefore, the associated state is only barely observable through the added two range outputs (last two rows). In addition, the fifth and sixth columns have a weaker relative contribution on the first output measurement than for navigation scenarios 1 and 2. Finally, the overall estimator performance might be significantly improved by the addition of this third range measurement because the density parameter is estimated here. This is demonstrated with the following navigation simulation.

C. Navigation Simulations

Similar to the previous navigation scenarios, a navigation simulation is conducted on the 3-DOF observation model of navigation scenario 3 to validate the observability analysis. As before, the simulation assumes the initialization of the state estimator with the values of Table 1 and the 10% modeling error on the atmospheric density and aerodynamic coefficients of the entry. Concerning the reference beacons, this simulation assumes a third fixed beacon on the planet surface at a different location than from the two other ground beacons at $\theta = -5.7$ deg, $\lambda = 5.7$ deg (more than 475 km from the other two ground beacons).

The 3-DOF simulation results for navigation scenario 3 are presented in Fig. 9 in the same fashion as was previously done for navigation scenario 1. The plots show that the L/D ratio is estimated accurately after the dynamic pressure has built up ($t > 50$ s). Furthermore, contrary to the previous scenarios, all six translational dynamics states are now accurately estimated. Therefore, the atmospheric modeling error that degraded the state estimation accuracy in the previous scenarios is overcome in this navigation scenario 3 by estimating the erroneous parameter along with the system states, although the reference density estimate shows an error of -10%. However, this density error is somewhat compensating for the $+10\%$ error on the ballistic coefficient that is not estimated in this model (Table 1).

In fact, it is not possible to observe B and ρ_0 independently with the observation model defined previously. For this reason, complementary plots are provided on Fig. 10 showing the product of the two parameters $B \times \rho_0$ to see if the product can be estimated correctly. As seen on the graphs, the estimation error becomes zero for navigation scenario 3 while the error for the IMU navigation scenario remains at 21% (both B and ρ_0 parameters start at 110% of their nominal value). Finally, this last result demonstrates that navigation scenario 3 using a third reference ranging measurement renders the state estimation even more accurate than navigation scenario 2 and enables estimation of the product $B\rho_0$.

D. Contribution Summary

In summary, navigation scenario 3 proposes three range measurements from known reference beacons to observe an atmospheric reference density parameter and cope for the state estimation inaccuracy observed in the previous scenarios. Thus, analyses and simulations showed that the atmospheric reference density could be estimated along with the other system states using the third range measurement.

VII. Navigation Scenario 4

The last navigation scenario analyzed consists of adding a third radio-ranging measurement to the previous navigation scenario 2. However, contrary to navigation scenario 3, this third range is measured from a beacon source with unknown position called the *proof mass*. In this novel entry navigation scenario, the lander would release this proof mass at the early stage of the hypersonic entry phase in order for both vehicles to benefit from the same initial entry conditions. The proof mass has no lift component, follows a free-falling ballistic trajectory, and is subject to the same atmospheric conditions as the main entry vehicle, at least during the first part of the trajectory.

As stated, the inertial position on this proof mass is not known to the lander navigation system. However, there is still a gain in

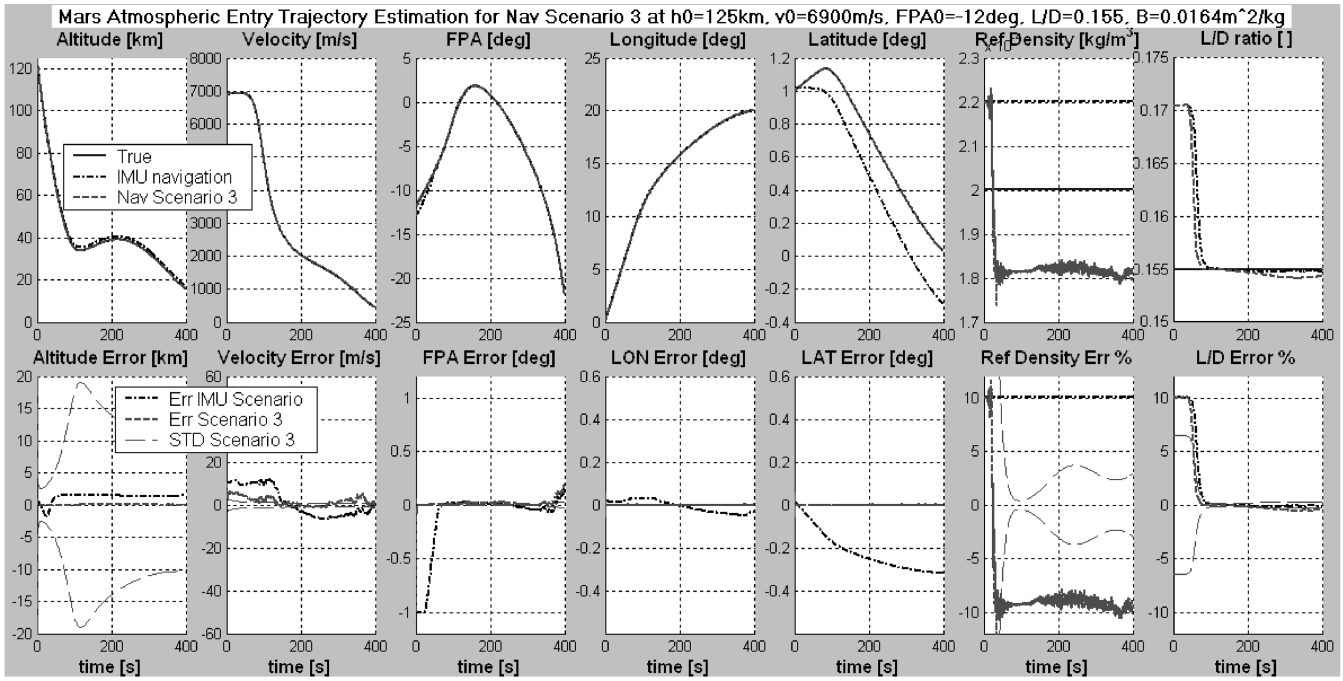

Fig. 9 State estimation comparison between IMU navigation and navigation scenario 3 with a 3-DOF atmospheric entry simulation for a vehicle with $L/D = 0.155$, $B = 0.016$ m^2/kg.

observability when the aerodynamic coefficients of this reference vehicle are perfectly known such as the coefficients of a sphere. The assumption is that any difference between the real and the modeled aerodynamics of the lander might be observed through the proof mass range measurement (Fig. 11), therefore allowing estimation of the lander aerodynamics although the position of the proof mass is unknown. This new navigation approach brings a major improvement to the estimator performance since the aerodynamics of the lander cannot be modeled accurately for the atmospheric environment of Mars.

For this proposed navigation scenario 4, the observation model is developed, analyzed with the observability matrix, and then simulated. Finally, two variants 4A and 4B of this scenario are presented and simulated.

A. Observation Model

The aerodynamic coefficients of the proof mass are easier to model (sphere) and are well known to the lander navigation system. The range equation between the lander and the proof mass is similar to the other range measurements and is defined as

$$\mathbf{R}_{\text{PM}} = \mathbf{r}_{\text{Lander}} - \mathbf{r}_{\text{PM}} \tag{29}$$

where the subscript PM denotes the proof mass. For this navigation scenario, two other range measurements from reference beacons are necessary to have a minimum observability of the nominal entry states, as per navigation scenario 2.

$$\mathbf{R}_{\text{Beacon1}} = \mathbf{r}_{\text{Lander}} - \mathbf{r}_{\text{Beacon1}} \qquad \mathbf{R}_{\text{Beacon2}} = \mathbf{r}_{\text{Lander}} - \mathbf{r}_{\text{Beacon2}} \tag{30}$$

Now, to figure out the dynamic interaction between the proof mass and the lander positions, the range dynamics are first described in a one-dimensional space in the following. Then, the results are transposed to a 3-DOF model.

1. 1-D Longitudinal Dynamics

The one-dimensional range dynamics is represented in Fig. 12. The two state equations for both objects are

$$\dot{s} = v \qquad \dot{v} = -d = -\tfrac{1}{2}B\rho v^2 \tag{31}$$

$$\dot{s}_{\text{PM}} = v_{\text{PM}} \qquad \dot{v}_{\text{PM}} = -d_{\text{PM}} = -\tfrac{1}{2}B_{\text{PM}}\rho_{\text{PM}}v_{\text{PM}}^2 \tag{32}$$

where s represents the 1-D position and the subscript PM represents the proof mass. In this one-dimensional space, the atmospheric density for both objects is the same and is assumed known. Also, the ballistic parameter B_{PM} is assumed constant and known. In contrast, B for the lander is constant but unknown. This lander ballistic coefficient becomes a new state in the system with dynamics

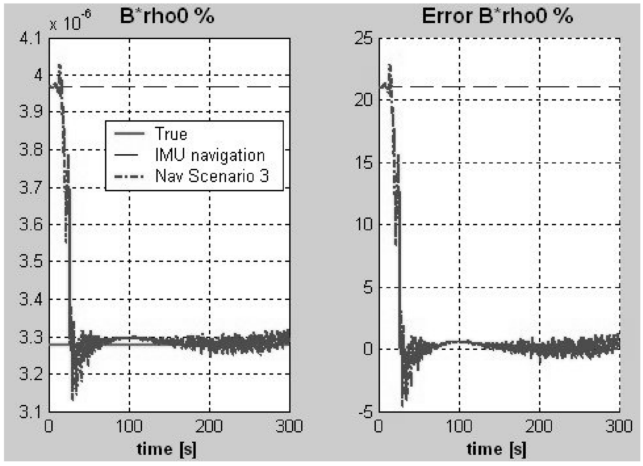

Fig. 10 Estimation of the parameter product $B^*\rho_0$ for navigation scenario 3.

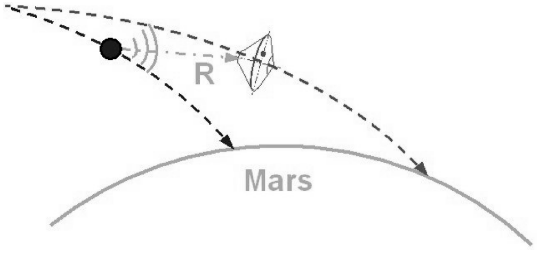

Fig. 11 Radio-ranging measurement from a free-falling proof mass.

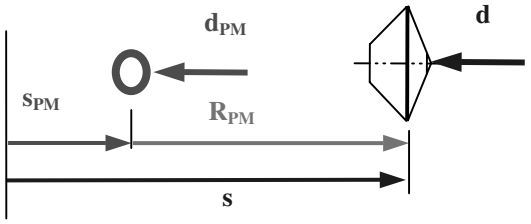

Fig. 12 One-dimensional representation of the range entry dynamics between the lander and the proof mass.

$$\dot{B} = 0 \tag{33}$$

Now, the range R_{PM} between the lander and the proof mass is reduced to

$$R_{\mathrm{PM}} = s - s_{\mathrm{PM}} \tag{34}$$

From this definition, the proof mass states Eq. (32) could be replaced by the relative range state equations

$$\dot{R}_{\mathrm{PM}} = \dot{s} - \dot{s}_{\mathrm{PM}} = v - v_{\mathrm{PM}} \qquad \ddot{R}_{\mathrm{PM}} = \dot{v} - \dot{v}_{\mathrm{PM}} = -d + d_{\mathrm{PM}} \tag{35}$$

After some manipulations and substitutions of the drag definition, the dynamics equations representing the five states $\{s, v, R_{\mathrm{PM}}, \dot{R}_{\mathrm{PM}}, B\}$ become

$$\begin{aligned} \dot{s} &= v \qquad \dot{v} = -\tfrac{1}{2}B\rho v^2 \qquad \dot{R}_{\mathrm{PM}} = \dot{R}_{\mathrm{PM}} \\ \ddot{R}_{\mathrm{PM}} &= -\tfrac{1}{2}B\rho v^2 + \tfrac{1}{2}B_{\mathrm{PM}}\rho_{\mathrm{PM}}(v - \dot{R}_{\mathrm{PM}})^2 \qquad \dot{B} = 0 \end{aligned} \tag{36}$$

In this one-dimensional space, $\rho = \rho_{\mathrm{PM}}$ and B_{PM} is known. Now, if the position s is known and the range R_{PM} is measured, the observability matrix analysis will tell that the system is completely observable. Hence the ballistic parameter B of the lander may be estimated accurately through the range measurement. However, IMU measurements will only give information on the acceleration of s instead of s itself, making this system only partially observable (therefore the need of complementary range measurements from reference beacons).

2. Three-DOF Observation Model

As seen for the 1-D model, with the addition of the proof mass range measurement, the ballistic coefficient of the entry vehicle may be estimated. However, by transposition of the 1-D model, in addition to this coefficient in state vector Eq. (14), two new states are required in the model, which are the range from the proof mass and its rate. Thus, for the 3-DOF model, the augmented system state vector is

$$\mathbf{x} = [\,r \quad v \quad \gamma \quad \psi \quad \theta \quad \lambda \quad L/D \quad R_{\mathrm{PM}} \quad \dot{R}_{\mathrm{PM}} \quad B\,]^T \tag{37}$$

Supposing that the velocity of the two vehicles remains collinear, the previous 1-D range dynamics yields for this 3-DOF model description. Thus,

$$\ddot{R}_{\mathrm{PM}} = -\tfrac{1}{2}B\rho v^2 + \tfrac{1}{2}B_{\mathrm{PM}}\rho_{\mathrm{PM}}(v - \dot{R}_{\mathrm{PM}})^2 \tag{38}$$

$$\dot{B} = 0 \tag{39}$$

where $B_{\mathrm{PM}} = 0.02\ \mathrm{m}^2/\mathrm{kg}$ is the known ballistic parameter of the proof mass and ρ_{PM} is the expected atmospheric density at the proof mass location. Equation (38) assumes that velocity of the lander and the proof mass are collinear, which is not really the case but this is a good preliminary approximation. For a proof mass tailing the entry vehicle ($B_{\mathrm{PM}} > B$), this last value may be approximated using the altitude difference computed from the range along the flight-path trajectory (Fig. 13):

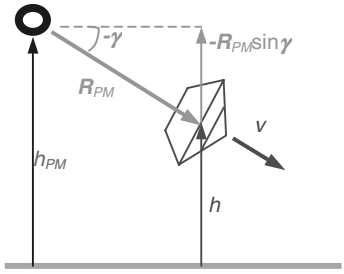

Fig. 13 Collinear approximation of the altitude at the proof mass location.

$$h_{\mathrm{PM}} \approx h - R_{\mathrm{PM}} \sin\gamma \tag{40}$$

Replacing this proof mass altitude into the exponential density model Eq. (6) yields

$$\rho_{\mathrm{PM}} = \rho \exp\left(\frac{-R_{\mathrm{PM}} \sin\gamma}{h_s}\right) \tag{41}$$

In the case where the proof mass is assumed falling ahead of the entry vehicle, the altitude is rather defined as

$$h_{\mathrm{PM}} \approx h + R_{\mathrm{PM}} \sin\gamma \tag{42}$$

However, the heat shield might prevent radio communication in this direction. Therefore, the first case is assumed using proof mass with an expected coefficient higher than the entry vehicle. Thus, the aerodynamic drag deceleration will be more important on the proof mass than on the lander and Eq. (40) will be used to represent the position of the proof mass behind the entry vehicle.

Now, the radio ranging provides the system with the range from two known reference beacons R_{Beacon1} and R_{Beacon2} and from the proof mass R_{PM}. Thus, in addition to the IMU measurements, observation outputs for the 3-DOF model become

$$\mathbf{y} = \begin{bmatrix} \mathbf{a}^B \\ R_{\mathrm{Beacon1}} \\ R_{\mathrm{Beacon2}} \\ R_{\mathrm{PM}} \end{bmatrix} \tag{43}$$

B. Observability Analysis

The same automated analysis as before is conducted on the augmented 3-DOF observation model for navigation scenario 3. The results are presented here. The added states are linearized by differentiation of Eqs. (38) and (39) with respect to the state vector Eq. (37):

$$\begin{aligned} \Delta\ddot{R}_{\mathrm{pm}} = \frac{\partial \ddot{R}_{\mathrm{pm}}}{\partial \mathbf{x}}\Delta\mathbf{x} + \frac{\partial \ddot{R}_{\mathrm{pm}}}{\partial \mathbf{u}}\Delta\mathbf{u} &= \left(\frac{d}{h_s} - \frac{\rho B_{\mathrm{pm}}(v - \dot{R})^2}{2h_s}\right)\Delta r \\ &- \left(\frac{2d}{v} - \rho B_{\mathrm{pm}}(v - \dot{R})\right)\Delta v - \rho B_{\mathrm{pm}}(v - \dot{R})\Delta\dot{R} - \frac{d}{B}\Delta B \end{aligned} \tag{44}$$

$$\Delta\dot{B} = \frac{\partial \dot{B}}{\partial \mathbf{x}}\Delta\mathbf{x} + \frac{\partial \dot{B}}{\partial \mathbf{u}}\Delta\mathbf{u} = 0 \tag{45}$$

Also, the other range measurement outputs are linearized by differentiation similar to the previous scenarios with respect to the state vector Eq. (37).

As usual, this linear dynamics is added to the previous linear observation model and the observability matrix is computed at different points along the trajectory. For this augmented system description, the analysis shows that the observability matrix of the linearized system is full rank at any linearization points along the trajectory, given $-90 < \lambda < 90$ deg. Hence, with the addition of the

proof mass range measurement to navigation scenario 2, the system 3-DOF entry dynamics augmented with the ballistic parameter is expected to be completely observable along the entire trajectory. A linear transformation into the JCF is not provided here since a Jordan matrix transformation was too complex to solve for the augmented dynamics Eq. (37) with the available computation tools (Matlab). However, the observability is assessed with the following navigation simulation.

C. Navigation Simulations

Similar to the previous navigation scenarios, a navigation simulation is conducted on the 3-DOF observation model of navigation scenario 4 in order to validate the observability analysis. As before, the simulation assumes the initialization of the state estimator with the values of Table 1 and the 10% modeling error on the atmospheric density and aerodynamic coefficients of the entry. Concerning the references, this simulation assumes the same two fixed reference beacons on the planet surface as per navigation scenario 2 and the proof mass that is located at the same initial position as the lander (Table 1) but having its own dynamics based on the same Eq. (1). The proof mass specific dynamics parameters are $B_{\mathrm{PM}} = 0.02\ \mathrm{m}^2/\mathrm{kg}$ and $L/D_{\mathrm{PM}} = 0$. Thus, the proof mass spherical configuration produces a slightly higher drag than the lander ($B = 0.016\ \mathrm{m}^2/\mathrm{kg}$) in order to be dragged behind the lander during the descent to be consistent with the range model represented in Fig. 13. Finally, this scenario represents the case where the proof mass would be softly released from the lander vehicle at the entry point.

Similar to navigation scenario 2, the 3-DOF simulation results presented in Fig. 14 show that the estimate of the state converges more toward the true state compared to navigation scenario 1. This was expected since both navigation scenarios 2 and 4 used two reference beacon range measurements. The gain in this last scenario compared to the former one is that the residual altitude and longitude errors are halved. This improvement is due to the observation of the modeling errors, but through the ballistic parameter estimation this time.

Effectively, it can be seen that the estimated error on the ballistic coefficient is less than 1%. Remaining errors are due to the one-dimensional proof mass range model Eq. (38) that is not accurate for the 3-DOF navigation because the lift vector that was unmodeled on the 1-D dynamics brings the lander and the proof mass on different trajectories (not collinear as the model assumed). Thus, the 1-D collinear range approximation becomes inaccurate at the end of the trajectory. A 3-D model of the range dynamics is not possible without losing observability because the position of the proof mass is unknown and this position state cannot be observed through the proposed measurements. Nevertheless, the state estimates remain closer to the true state than for navigation scenarios 1 and 2 and this result demonstrates the navigation improvement through the addition of the proof mass ranging.

Finally, this simulation validates the observability analysis and demonstrates that navigation scenario 4 using a proof mass ranging measurement renders the state estimation more accurate and enables estimation of the lander ballistic coefficient.

D. Scenario Variant 4A

A first variant to this scenario is proposed to remove the two reference beacon range measurements from navigation scenario 4 and keep only the IMU and the range measurement from the proof mass. This navigation scenario 4A may be useful to see how the default navigation scenario is improved when the lander ballistic parameter is estimated through the proof mass ranging.

Similar to the previous scenarios, a navigation simulation is conducted on the 3-DOF observation model of this scenario variant. The results for the 3-DOF simulation presented in Fig. 15 show that the ballistic parameter may be estimated through the proof mass ranging. Finally, this simulation demonstrates similar improvement on the altitude estimate from the default scenario as observed previously between navigation scenarios 2 and 4.

E. Scenario Variant 4B

A second variant to this scenario is proposed to combine both the improvements of navigation scenarios 3 and 4. Thus, a range measurement from a third reference beacon is added to the last scenario order to achieve reference density estimation as per navigation scenario 3. Here, the state dynamics are thus augmented with the parameter ρ_0 and the observation model is augmented with the third range R_{Beacon3}.

Similar to the previous scenarios, a navigation simulation is conducted on the 3-DOF observation model of this augmented navigation scenario 4B. The results for the 3-DOF simulation

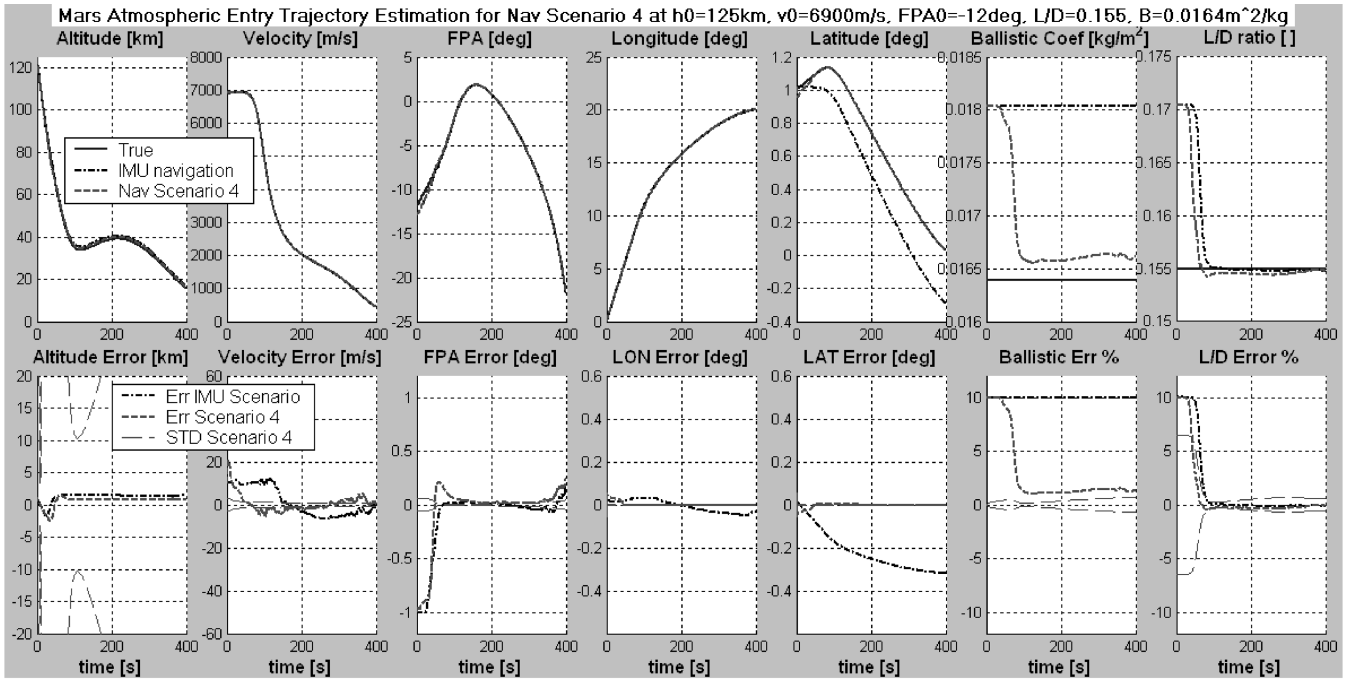

Fig. 14 State estimation comparison between IMU navigation and navigation scenario 4 with a 3-DOF atmospheric entry simulation for a vehicle with $L/D = 0.155$, $B = 0.016\ \mathrm{m}^2/\mathrm{kg}$.

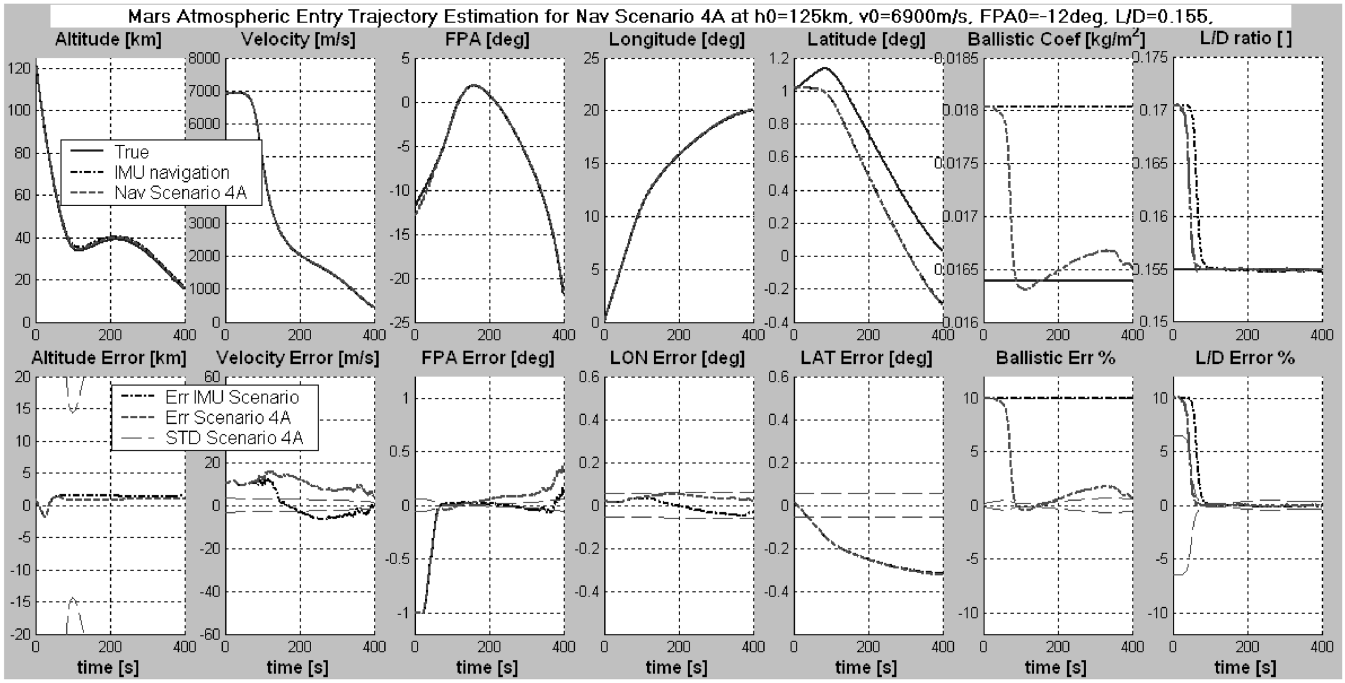

Fig. 15 State estimation comparison between IMU navigation and navigation scenario 4A variant with a 3-DOF atmospheric entry simulation for a vehicle with $L/D = 0.155$, $B = 0.016$ m^2/kg.

presented in Fig. 16 demonstrate almost perfect state and parameter estimation after less than 30 s compared to the default IMU-based navigation. This scenario variant constitutes the last and most promising contribution on navigation techniques for Mars atmospheric entry.

F. Contribution Summary

In summary, navigation scenario 4 proposes an innovative way for ranging from a reference with unknown position called the proof mass. This no-lift spherical proof mass is released from the lander during entry and follows the lander in an unguided ballistic flight. Because the proof mass with known aerodynamics travels under the same atmospheric conditions as the primary vehicle, the ranging dynamics between the two objects enabled the observation of the ballistic coefficient of the lander. This is successfully demonstrated with observability analyses and navigation simulations on the 3-DOF, particularly when the system aerodynamics is not perfectly modeled.

Finally, to easily picture this contribution with respect to the previous ones, all the navigation scenario contributions have been summarized in Table 2. Their respective performance is represented

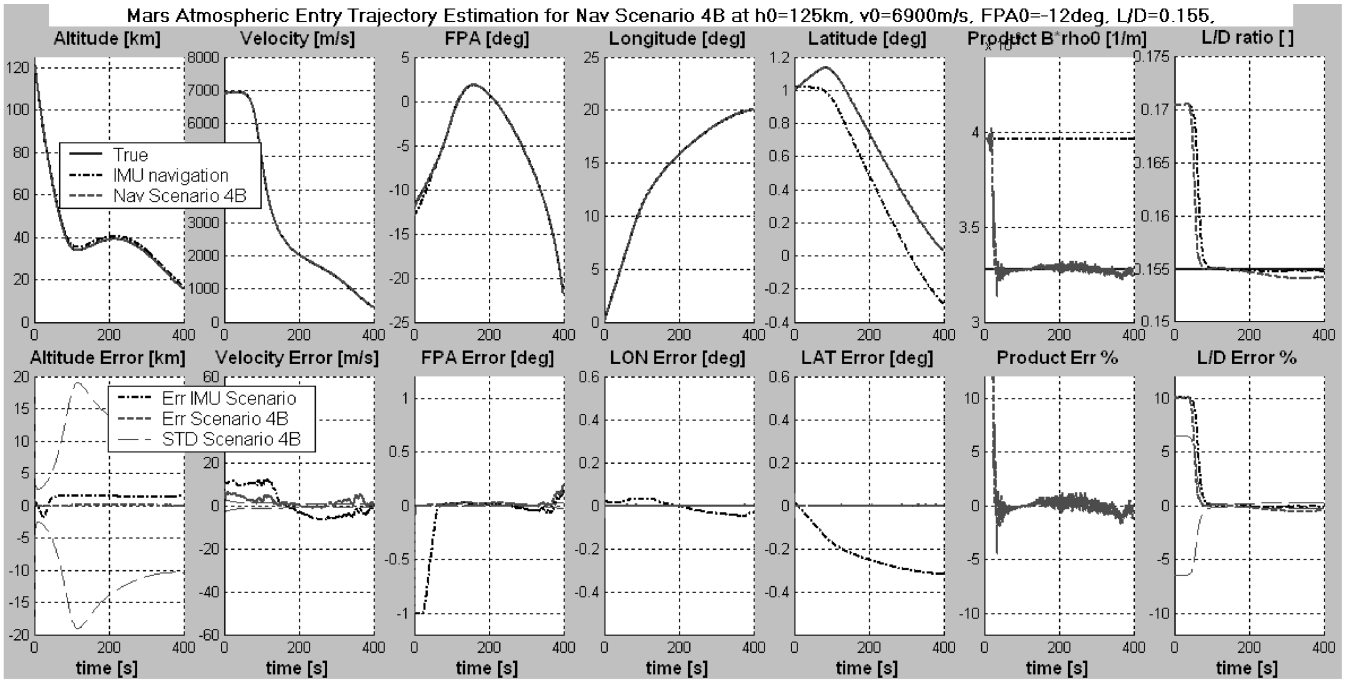

Fig. 16 State estimation comparison between IMU navigation and navigation scenario 4B variant with a 3-DOF atmospheric entry simulation for a vehicle with $L/D = 0.155$, $B = 0.016$ m^2/kg.

Table 2 Summary of the navigation scenario contributions

Contribution	Measurements			State	Parameter identification		
scenario	IMU	No. range	Proof mass	convergence	L/D	B	ρ_0
Default nav. scenario	3-axis accel.	0	No	2/6	Yes	No	No
Nav. scenario 1	3-axis accel.	1	No	3/6	Yes	No	No
Nav. scenario 2	3-axis accel.	2	No	5/6	Yes	No	No
Nav. scenario 3	3-axis accel.	3	No	6/6	Yes	No	Yes
Nav. scenario 4	3-axis accel.	2	Yes	5/6	Yes	Yes	No
Nav. scenario 4A	3-axis accel.	0	Yes	2/6	Yes	Yes	No
Nav. scenario 4B	3-axis accel.	3	Yes	6/6	Yes	Yes	Yes

by the number of converged states and parameters during the navigation simulations.

VIII. Conclusions

This paper reviewed the atmospheric entry dynamics observability for the default case navigation system using IMU measurements only. Observability analyses and navigation simulations on the default navigation scenario showed that IMU measurements only are not sufficient for high-precision navigation.

To achieve pinpoint precision landing on Mars, the first step of this work was the implementation of the unscented Kalman filter techniques for state estimation during atmospheric entry. The second step was the investigation of novel navigation scenarios to improve the observability of the system. Among the possible sensor technologies, radio communication revealed that one-way radio ranging from emitting beacons might be efficiently used for navigation. Thus, four navigation scenarios with increasing number of range measurements are proposed to address the observability problem. Depending on the scenario configuration, it is demonstrated through analyses and simulations that complete observability of the states can be achieved as well as the identification of some critical model parameters such as the lift-to-drag ratio, the ballistic coefficient, and the reference atmospheric density.

In summary, the additional range measurements allow the observation of modeling errors and the accurate estimation of the system states and parameters to reduce the landing dispersions for precision landing on Mars. Practical implementation of such a navigation system using a single known reference radio beacon is currently under investigation for the MSL mission. Future work may consider implementation and the financial aspect for using more than one beacon or the proof mass concept developed in this paper.

Appendix: Observability Analysis Tools

For an estimator to converge, all the states used in the observation model must be observable, in which case complete observability of the system is obtained. If one or more states cannot be observed through the available measurements, only partial observability of the system is obtained. In this case, some states may diverge during estimation and the estimator may become unstable. Following is a description of observability tools that may be used in this sense.

A. Observability Matrix

For a continuous-time state-space description of a system in the form

$$\dot{\mathbf{x}} = \mathbf{A}\mathbf{x} + \mathbf{B}\mathbf{u} \qquad \mathbf{y} = \mathbf{C}\mathbf{x} + \mathbf{D}\mathbf{u} \tag{A1}$$

where $\mathbf{x} \in \Re^n$ is the state, $\mathbf{u} \in \Re^m$ the input, and $\mathbf{y} \in \Re^P$ the output, the observability matrix $\mathbf{Q}_0$ is defined as

$$\mathbf{Q}_0 = \begin{bmatrix} \mathbf{C} \\ \mathbf{C}\mathbf{A}^1 \\ \cdots \\ \mathbf{C}\mathbf{A}^n \end{bmatrix} \tag{A2}$$

where n is the order of the system. When the rank of the matrix is equal to the dimension n of the state, the system is then completely observable (Ogata, 1997 [20]). This tool is simple and does not require specific properties of the system such as stability for its application. However, the system must be expressed in the linear form (A1). Before analysis of their observability using Eq. (A2), nonlinear systems have to be linearized about an operational point with the following first-order Taylor series approximation:

$$\mathbf{x} = \mathbf{x}_0 + \Delta\mathbf{x} \qquad \mathbf{y} = \mathbf{y}_0 + \Delta\mathbf{y} \qquad \mathbf{u} = \mathbf{u}_0 + \Delta\mathbf{u} \tag{A3}$$

$$\begin{aligned} \Delta\dot{\mathbf{x}} &= \frac{\partial f(\mathbf{x},\mathbf{u})}{\partial \mathbf{x}}\Delta\mathbf{x} + \frac{\partial f(\mathbf{x},\mathbf{u})}{\partial \mathbf{u}}\Delta\mathbf{u} = \mathbf{A}\Delta\mathbf{x} + \mathbf{B}\Delta\mathbf{u} \\ \Delta\mathbf{y} &= \frac{\partial h(\mathbf{x},\mathbf{u})}{\partial \mathbf{x}}\Delta\mathbf{x} + \frac{\partial h(\mathbf{x},\mathbf{u})}{\partial \mathbf{u}}\Delta\mathbf{u} = \mathbf{C}\Delta\mathbf{x} + \mathbf{D}\Delta\mathbf{u} \end{aligned} \tag{A4}$$

where $\mathbf{x}_0$, $\mathbf{y}_0$, and $\mathbf{u}_0$ denote the state, the output, and the input at the linearization point.

B. Jordan Canonical Form

Because the observability matrix analysis only provides the number of observable states through the rank of the matrix, which may also be dependant on numerical approximations, it does not directly indicate the relative degree of observability for each state. To quantify the observability of the states with respect to the output measurements, the state-space system can be transformed into the JCF as follows:

$$\bar{\mathbf{x}} = \mathbf{V}\mathbf{x} \qquad \bar{\mathbf{A}} = \mathbf{V}^{-1}\mathbf{A}\mathbf{V} \qquad \bar{\mathbf{B}} = \mathbf{V}^{-1}\mathbf{B} \qquad \bar{\mathbf{C}} = \mathbf{C}\mathbf{V} \tag{A5}$$

where the bar indicates the transformed parameter such that

$$\dot{\bar{\mathbf{x}}} = \bar{\mathbf{A}}\,\bar{\mathbf{x}} + \bar{\mathbf{B}}\mathbf{u} \qquad \mathbf{y} = \bar{\mathbf{C}}\,\bar{\mathbf{x}} + \mathbf{D}\mathbf{u} \tag{A6}$$

and $\mathbf{V}$ is the linear transformation matrix obtained through the Jordan diagonal solution:

$$\mathbf{A}\mathbf{V} = \mathbf{V}\mathbf{J} \tag{A7}$$

where $\mathbf{J}$ is the Jordan diagonal matrix containing the eigenvalues of the system.

In the JCF, the output matrix $\bar{\mathbf{C}}$ can show how the transformed states $\bar{\mathbf{x}}$ are connected to each output. If a column of the matrix is found to contain only very small numbers compared to the other columns, then the outputs are not influenced by the associated state. Therefore, this state may be considered only barely observable. This gives a more relevant conclusion on the observability of a system for which the observability matrix might otherwise indicate that the system is completely observable.

Acknowledgments

This work is supported in part by the following grants: NSERC ESD2-303668, CSA Supplement ESD2-303668, and FQRNT 101615.

References

[1] Spencer, D. A., and Braun, R. D., "Mars Pathfinder Atmospheric Entry: Trajectory Design and Dispersion Analysis," *Journal of Spacecraft and Rockets*, Vol. 33, No. 5, Sept. 1996, pp. 670–676.

[2] Desai, P. N., and Knocke, P. C., "Mars Exploration Rovers Entry, Descent and Landing Trajectory Analysis," AIAA Paper 2004-5092, Aug. 2004.

[3] Wolf, A. A., Graves, C., Powell, R. W., and Johnson, W., "Systems for Pinpoint Landing at Mars," *Proceedings of the 14th AAS/AA Space Flight Mechanics Meeting*, Jet Propulsion Laboratory, California Institute of Technology, American Astronomical Society, Washington, D.C., 2004, AAS 04-272.

[4] de Lafontaine, J., and Gueye, O., "Autonomous Planetary Landing Using a LIDAR Sensor: The Navigation Function," *Space Technology*, Vol. 24, Nos. 00–12, 2003, pp. 147–157.

[5] Lu, P., "Entry Guidance and Trajectory Control for Reusable Launch Vehicle," *Journal of Guidance, Control, and Dynamics*, Vol. 20, No. 1, 1997, pp. 143–149.

[6] Lu, P., and Hanson, J. M., "Entry Guidance for the X-33 Vehicle," *Journal of Spacecraft and Rockets*, Vol. 35, No. 3, 1998, pp. 342–349.

[7] Lu, W.-M., and Bayard, D. S., "Guidance and Control for Mars Atmospheric Entry: Adaptivity and Robustness," Technical Report, Jet Propulsion Lab., California Institute of Technology, Pasadena, CA, 1997STIN-0060813L.

[8] Masciarelli, J. P., Rousseau, S., Fraysse, H., and Perot, E., "An Analytic Aerocapture Guidance Algorithm for the Mars Sample Return Orbiter," AIAA Paper 2000-4116, Aug. 2000.

[9] Mease, K. D., Chen, D. T., Tandon, S., Young, D. H., and Kim, S., "A Three-Dimensional Predictive Entry Guidance Approach," AIAA Paper 2000-3959, 2000.

[10] Mease, K. D., Chen, D. T., Teufel, P., and Schonenberger, H., "Reduced-Order Entry Trajectory Planning for Acceleration Guidance," *Journal of Guidance, Control, and Dynamics*, Vol. 25, No. 2, 2002, pp. 257–266.

[11] Mease, K. D., and Kremer, J-P., "Shuttle Entry Guidance Revisited Using Nonlinear Geometric Methods," *Journal of Guidance, Control, and Dynamics*, Vol. 17, No. 6, 2004, pp. 1350–1356.

[12] Powell, R. W., "Six-Degree-of-Freedom Guidance and Control-Entry Analysis of the HL-20," *Journal of Spacecraft and Rockets*, Vol. 30, No. 5, 1993, pp. 537–544.

[13] Powell, R. W., and Braun, R. D., "Six-Degree-of-Freedom Guidance and Control Analysis of Mars Aerocapture," *Journal of Guidance, Control, and Dynamics*, Vol. 16, No. 6, 1993, pp. 1038–1044.

[14] Powell, R. W., "Numerical Roll Reversal Predictor-Corrector Aerocapture and Precision Landing Guidance Algorithms for the Mars Surveyor Program 2001 Mission," AIAA Paper 98-4574, Aug. 1998.

[15] Jah, M., Lisano, M., Born, G., and Axelrad, P., "Mars Aerobraking Spacecraft State Estimation by Processing Inertial Measurement Unit Data," Ph.D. Dissertation, University of Colorado, Aug. 2005.

[16] Levesque, J.-F., "Advanced Navigation and Guidance for High Precision Planetary Landing on Mars," Ph.D. Thesis, Department of Electrical Engineering, Université de Sherbrooke, Aug. 2006.

[17] Riedel, B., Desai, H., Kennedy, N., Synnott, W., and Werner, Z., "Autonomous Optical Navigation—DS1 Technology Validation Report," JPL, California Institute of Technology, Pasadena, CA.

[18] Rayman, M. D., Varghese, P., Lehman, D. H., and Livesay, L. L., "Results from the Deep Space 1 Technology Validation Mission," *50th International Astronautical Congress*, International Astronautical Federation, Paris, IAA-99-IAA.11.2.01, 1999; also *Acta Astronautica*, No. 47, 2000, p. 475.

[19] Polle, F., Voirin, G.-F., Rebordao, C., Proenca, M., Graziano, P., and Motrena, D., "Vision Based Navigation for Planetary Exploration Opportunity for AURORA," *54th International Astronautical Congress*, International Astronautical Federation, Paris, 2003.

[20] Ogata, K., *Modern Control Engineering*, 3rd ed., Prentice–Hall, Upper Saddle River, NJ, 1997, pp. 997, 998.

[21] Julier, S. J., and Uhlmann, J. K., "A New Extension of the Kalman Filter to Nonlinear Systems," *Proceedings of the AeroSense: The 11th International Symposium on Aerospace/Defence Sensing, Simulation and Controls*, 1997.

[22] Wan, E., and van der Merwe, R., "The Unscented Kalman Filter for Nonlinear Estimation," *Proceedings of the IEEE Symposium 2000 (AS-SPCC)*, IEEE, Piscataway, NJ, 2000.

[23] Julier, S. J., and Uhlmann, J. K., "Reduced Sigma Point Filters for the Propagation of Means and Covariance Through Nonlinear Transformations," Report, IDAK Industries, Jefferson City, MO, 1998.

[24] Julier, S. J., "The Scaled Unscented Transformation," *American Control Conference*, IEEE, Piscataway, NJ, 2000, ISSN 0743-1619.

[25] Van der Merwe, R., and Wan, E., "The Square-Root Unscented Kalman Filter for State and Parameter-Estimation," *Proceedings of the International Conference on Acoustics, Speech, and Signal Processing (ICASSP)*, IEEE, Piscataway, NJ, 2001.

[26] Van der Merwe, R., and Wan, E., "Sigma-Point Kalman Filters for Probabilistic Inference in Dynamic State-Space Models," OGI School of Science & Engineering, Oregon, 2000.

[27] Levesque, J.-F., "Second-Order Simplex Sigma Points for Nonlinear Estimation," *AIAA Conference on Guidance, Navigation and Control*, AIAA, Reston, VA, 2006.

[28] Burkhart, P. D., Ely, T., Duncan, C., Lightsey, E. G., Campbell, T., and Mogensen, A., "Expected EDL Navigation Performance with Spacecraft to Spacecraft Radiometric Data," AIAA Paper 2005-6435, Aug. 2005.

[29] Burkhart, P. D., Ely, T., Duncan, C., Lightsey, E. G., Campbell, T., and Mogensen, A., "Real-Time EDL Navigation Performance Using Spacecraft to Spacecraft Radiometric Data," AIAA Paper 2006-6566, 2006.

[30] Lau, K., Lichten, S., Young, L., and Haines, B., "An Innovative Deep Space Application of GPS Technology for Formation Flying Spacecraft," AIAA Paper 96-3819, July 1996.

[31] Morabito, D. D., "The Spacecraft Communications Blackout Problem Encountered During Passage or Entry of Planetary Atmospheres," Jet Propulsion Laboratory, IPN Progress Report 42-150, NASA, Aug. 2002.